Numerical study of the counterflow diffusion flames of methanol hydrothermal combustion
The real-fluid effects and flamelet analysis

Ren, Mengmeng; Wang, Shuzhong; Roekaerts, Dirk

Important note
To cite this publication, please use the final published version (if applicable).
Please check the document version above.

Numerical study of the counterflow diffusion flames of methanol hydrothermal combustion: the real-fluid effects and flamelet analysis

Mengmeng Ren [a,b,*], Shuzhong Wang [b], Dirk Roekaerts[a,*]

[a]Department of Process and Energy, Delft University of Technology, Leeghwaterstraat 39, 2628 CB Delft, The Netherlands

[b] Key Laboratory of Thermo-Fluid Science and Engineering of MOE, School of Energy and Power Engineering of Xi'an Jiaotong University, Xi'an, Shaanxi 710049, China

*Corresponding Author.

Email address: ren.meng.meng@163.com (M. Ren); szwang@aliyun.com (S. Wang); D.J.E.M.Roekaerts@tudelft.nl (D. Roekaerts).

Abstract (100-150 words)

The counterflow diffusion flames of methanol hydrothermal combustion are investigated to improve the understanding of hydrothermal flames. It is indicated that the thermodynamic properties by Peng-Robinson equation of state and the polynomial fitted viscosity and thermal conductivity can reduce the flame temperature by about 500K. The Takahashi correlation for mass diffusivity is found to be appropriate through comparison with the experimental data of Wellig et al. (*J. Supercrit. Fluids, 2009, 49, 1*). By comparing with the Kolmogorov length scale in the practical combustor, the thickness of the calculated counterflow flame is ten times larger, which means that the flame is affected by the turbulence intensively. The flame stable range is also reproduced well by the developed hydrothermal counterflow flame model. In the end, an Flamelet Generated Manifold (FGM) table is generated, promising to provide good closure of the non-equilibrium chemical source term in further turbulent flame simulations.

Keyword

Hydrothermal combustion; Counterflow flames; real-fluid properties; FGM (Flamelet Generated Manifold) model; flamelet; SCWO (Supercritical Water Oxidation)

1   Introduction

Hydrothermal combustion denotes the combustion process occurring in supercritical water, where the pressure is higher than the critical pressure of water (22.1MPa) [1]. The first hydrothermal flame was produced by Frank et al.[2] in 1988. Then this special type of combustion has been investigated mainly in the field of SCWO (supercritical water oxidation) [3-5], which is a wet waste treatment technology. Supercritical water provides a favourable environment for the oxidation of organic waste. Most organics and nonpolar molecules can be dissolved well in supercritical water, which eliminates the transport barrier at the phase interface. Hydrothermal flames can provide an internal heat source in the SCWO reactor, which is favourable for the process in many ways, for example, the lower preheat temperatures, the less corrosion/plug problems and the higher energy output [6-8]. On the other hand, if the hydrothermal flame is generated by an auxiliary fuel, abundant free radicals in the flame can promote the oxidation of the refractory organic wastes [9].

The ignition and extinction limits are always the main concerns in the hydrothermal combustion research [10-14]. Developing a numerical method, which can predict the ignition and extinction, is of importance for the design and optimization of practical reactors. Narayanan et al. [15] have modelled the ETH (Swiss Federal Institute of Technology) hydrothermal burner [12] with the eddy-dissipation (ED) model. The position of the flame was well reproduced, while the temperature rise was over-predicted by 15-18%. Sierra-Pallares et al. [16] have used the multiple-time-scale (ED-MTS) turbulent mixing model [17], which use the scalar dissipation time scale instead of the fluid dynamic dissipation time scale,

to account for the large Schmidt number and longer mixing time occurred in hydrothermal flames. It is showed that the ED-MTS model can decrease the average deviation between the ETH experimental temperature and the predicted value to 5-10%. These models are able to simulate the fast chemistry conditions where reaction rate is limited by the turbulent mixing, but they fail to simulate the ignition and extinction conditions where chemical kinetics plays an important role. Queiroz et al. [18] have used a one-step finite rate reaction model to simulate the premixed hydrothermal flames in their vessel reactors. In our previous research [19], the finite-rate/eddy-dissipation model was applied to the ETH burner, by which the ignition and extinction limits were addressed. However, the extinction temperature was under-predicted by 250K, which is mainly due to the inaccurate turbulence-chemistry interaction model.

Study of counterflow flames with detailed chemistry can provide detailed information about the laminar flame structure, and on the other hand, can generate flamelet-based manifold which is promising to provide better closure of the mean chemical source term in turbulent flame simulation [20-25]. The counterflow flame at hydrothermal condition is seldomly studied. The closest branch in the combustion field is the supercritical combustion in rocket engines [26-28]. Ribert et al. [29] have investigated the counterflow diffusion flame of hydrogen for subcritical and supercritical pressure, which showed that the flame thickness and heat release rate are inversely correlated with the product of pressure and strain rate while the extinction strain rate increases with the pressure. Lacaze and Oefelein [30] have found that the presence of water in the supercritical hydrogen/oxygen flame significantly increases the critical pressure of the mixture. One difference between the hydrothermal combustion with the supercritical hydrogen combustion is just that the mass fraction of supercritical water in hydrothermal flames is always more than 50%. Very recently, Gao et al. [31] conducted a priori and a posteriori tests on the flamelet library generated by real-fluid steady flamelet

equations with the unity Lewis number assumption at hydrothermal conditions. It was shown that the flamelet library can properly reproduce the laminar hydrothermal flames calculated by a 2-D simulation with detailed chemistry. More analysis of the hydrothermal counterflow flames needs to be conducted, for example the effect of real-fluid mass diffusivity, the comparison with experiments and the evaluation of the turbulence-chemistry interactions.

In this work, a comprehensive study is conducted on the methanol counterflow flame at hydrothermal conditions. Firstly, the effect of the real-fluid thermodynamic and transport properties on the flame structure are illustrated separately. The sensitivity of the flame to the mass diffusion coefficients is also investigated to come to a proper choice of the mass diffusion model. Secondly, the calculated results are compared with the ETH experimental data, including flame temperature and the extinction limits. The turbulence scale of the ETH combustor is also analysed by comparison with the laminar counterflow flame thickness, to assess the intensity of the turbulence and chemistry interaction. Finally, an FGM (Flamelet Generated Manifold) table is generated from the combination of steady and unsteady counterflow flames calculations, which will provide the thermochemistry database for further simulation of turbulent hydrothermal flames.

2 Model and Method
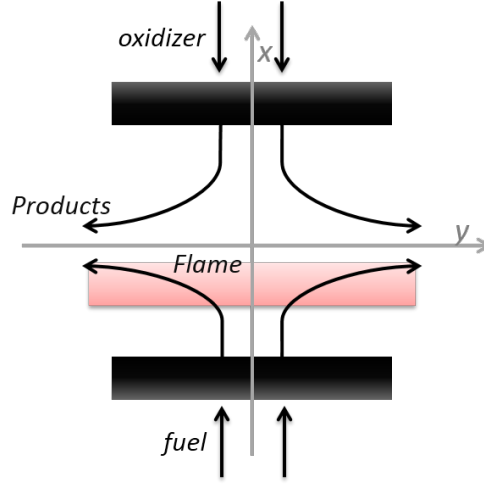
2.1 Governing equations

Fig. 1 Sketch of the counterflow diffusion flame

In the counterflow diffusion flame fuel and oxidizer come from opposite ducts and mix by

mass diffusion (see Fig. 1). Let u and v denote velocity components in x and y direction

(indicated in Fig. 1). By defining the stretch term as $K = \partial v / \partial y$, the transport equations

governing the flow can be written as the following set of one-dimensional equations [32]:

$$
\frac{\partial \rho}{\partial t} + \frac{\partial (\rho u)}{\partial x} = -\rho K
$$

$$
\frac{\partial (\rho Y_i)}{\partial t} + \frac{\partial (\rho u Y_i)}{\partial x} = \frac{\partial}{\partial x}\left(\rho D_{im} \frac{\partial Y_i}{\partial x} \right) + \dot{\omega} - \rho K Y_i
$$

$$
\frac{\partial \rho h}{\partial t} + \frac{\partial (\rho u h)}{\partial x} = \frac{\partial}{\partial x}\left[\frac{\lambda}{c_p} \frac{\partial h}{\partial x} + \sum_{i=1}^{N_s}\left(\rho D_{im} - \frac{\lambda}{c_p} \right) h_i \frac{\partial Y_i}{\partial x} \right] - \rho K h
$$

$$
\rho \frac{\partial K}{\partial t} + \rho u \frac{\partial K}{\partial x} = \frac{\partial}{\partial x}\left(\mu \frac{\partial K}{\partial x} \right) - \rho K^2 + \rho_2 a^2
$$

(1)

in which t, Y_i, and h denote the time, mass fraction of species i and the enthalpy. ρ, D_{im}, $\dot{\omega}$,

λ, C_p and μ denote the density, the mixture mass diffusion coefficient, the reaction rate, the

thermal conductivity, the heat capacity and the viscosity. a and ρ_2 is the applied strain rate

and the density at the oxidizer side. The methods to calculate the thermodynamic and

transport properties are well-established for the case of an ideal gas and implemented in many

1-D flame codes, for example the CHEM1D code [33] which is used in this work. However,

at hydrothermal conditions, all these methods should be modified to be suitable for

supercritical fluids. In the following part, real-fluid modifications on the thermodynamic and transport properties will be evaluated. The ideal gas values plotted for comparisons are obtained by the method described in reference [34].

2.2 Equation of state and thermodynamic properties

The ideal gas equation of state is replaced by Peng-Robinson equation of state (EOS) [35] to account for the real-fluid thermodynamic properties at hydrothermal conditions. It takes the form:

$$P = \frac{RT}{v-b} - \frac{\alpha(T)}{v^2 + 2bv - b^2}$$

(2)

where R is the universal gas constant, $\alpha(T)$ and b are parameters as function of the properties of the mixture:

$$\alpha(T) = \alpha_0 [1 + n(1 - (T/T_c)^{0.5})]^2 \qquad \alpha_0 = \frac{0.45724 R^2 T_c^2}{P_c}$$

$$n = 0.37464 + 1.54226\omega - 0.26992\omega^2 \qquad b = \frac{0.07780 R T_c}{P_c}$$

(3)

in which T_c, P_c, ω denote the critical temperature, the critical pressure and the acentric factor respectively. The method to calculate these properties of the mixture is adopted from Evlampiev's work [] as:

$$T_c = \sum_i X_i T_{c,i} \qquad P_c = \sum_i X_i P_{c,i} \qquad \omega = \sum_i X_i \omega_i$$

(4)

where X_i is the mole fraction of the species i, $T_{c,i}$, $P_{c,i}$ and ω_i are the critical temperature, the critical pressure and the acentric factor of species i.

The enthalpy of each species is modified as a sum of the ideal gas value and a residue term which can be deduced from the Peng-Robinson EOS:

$$h = h^{id} + h^{resi}$$

(5)

$$h^{resi} = \int_{\infty}^{v} \left[T\left(\frac{\partial P}{\partial T}\right)_v - P \right] dv + Pv - RT$$
$$= \frac{\alpha(T) - T\alpha'(T)}{2\sqrt{2}b} \ln \frac{V - \sqrt{2}b + b}{V + \sqrt{2}b + b} + PV - RT$$

(6)

Accordingly, the real-fluid heat capacity is calculated from the derivative of enthalpy:

$$C_p = C_p^{\ id} + C_p^{\ resi}$$

(7)

$$C_p^{\ resi} = \left(\frac{\partial h^{resi}}{\partial T}\right)_p = \left(\frac{h^{resi}(T + 0.01K) - h^{resi}(T)}{0.01K}\right)_p$$

(8)

2.3 Transport properties

The value of transport properties can have large influence on the diffusion flame structure. In this work, viscosity and thermal conductivity of the mixture are evaluated for the main species including water, methanol, carbon dioxide and oxygen. Because the sum of the mass fraction of these four species is always larger than 90%, we suppose that the viscosity and thermal conductivity of the mixture are not affected too much by other species. However, the mass diffusivity controls supply of reactants locally in the flame and in order to be accurate should be specified individually for each species also minor species. Hence, a comprehensive evaluation will be conducted for mass diffusivities to find a proper model applied for every species.

2.3.1 Viscosity and thermal conductivity

The viscosity and thermal conductivity of four main species calculated by ideal gas model and looked up from a NIST database [36] are both plotted in Fig. 2, as function of temperature at pressure of 25MPa. It shows that the ideal gas model would largely under-predict the viscosity and thermal conductivity at the temperature range near and below the critical

temperature. For reference, the critical pressure and temperature for main species are listed in Table 1 Critical properties of main species.

In this work we have refitted the viscosities and thermal conductivities over the whole temperature range, to replace the old polynomial coefficients for ideal gas in the CHEM1D input file [34]. For the thermal conductivity of water and methanol, piecewise polynomial fitting is conducted to get better agreement. The results from the new polynomial fittings are also plotted in Fig. 2, with the average absolute value of the relative deviation labelled for each polynomial fitting.

The viscosity and thermal conductivity of the mixture is calculated by the mixing law:

$$\mu = \sum_{i=1}^{N_s} \frac{\mu_i}{1+X_i^{-1}\sum_{j=1,j\neq i}^{N_s}X_j\Phi_{ij}} \qquad \Phi_{ij} = \frac{1}{\sqrt{8}}\left(1+\frac{M_i}{M_j}\right)^{-1/2}\left[1+\left(\frac{\mu_i}{\mu_j}\right)^{1/2}\left(\frac{M_j}{M_i}\right)^{1/4}\right]^2 \qquad (9)$$

$$\lambda = \frac{1}{2}\left[\sum_{i=1}^{N}X_i\lambda_i + \left(\sum_{i=1}^{N}X_i/\lambda_i\right)^{-1}\right] \qquad (10)$$

where μ_i, λ_i and M_i are the viscosity, the thermal conductivity and the molar mass of species i. The relative deviation between the value only considering the real-fluid modification on the four main species and the value considering all species is lower than 3%.

Table 1 Critical properties of main species

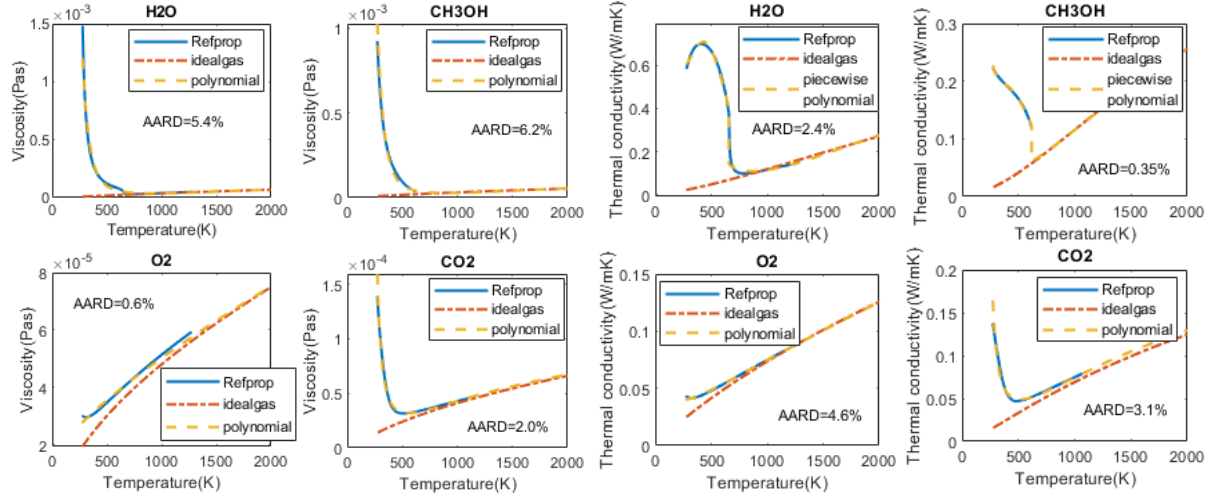|	H_2O	CH_3OH	O_2	CO_2
P_c(MPa)	22.1	8.2	5.0	7.4
T_c(K)	647.1	512.6	154.6	304.2

Fig. 2 Viscosity and thermal conductivity of main species predicted by different models at pressure of 25MPa.

2.3.2 Mass diffusivity

Kraft and Vogel [37] reviewed the existing formulas for mass diffusivity in supercritical

water, and the calculated values were compared with either experimental or molecular

simulation results. They concluded that the Wilke-Chang formula is more suitable for

conditions near the critical point (647K, 22.1MPa), while the Stokes-Einstein equation is

suggested for conditions above the critical point (673K and 773K, 30.0MPa). For combustion

calculations values are needed at higher temperature. The mass diffusivity of oxygen in

supercritical water predicted by these two equations at 25 MPa over a wide temperature range

is shown in Fig. 3. It can be seen that the Stokes-Einstein and Wilke-Chang formulas predict

diffusivity values that are around ten times lower than the ideal gas value. The ideal gas value

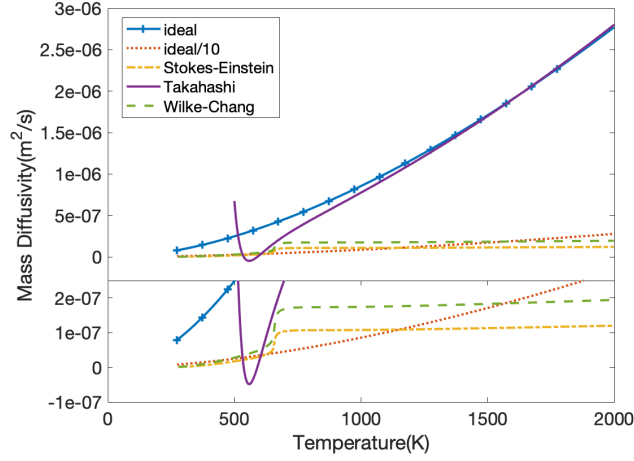and 1/10 of the ideal gas value are also plotted as a reference.

Fig. 3 Mass diffusivity of oxygen in water at 25MPa calculated by different formulas

On the other hand, in the research of supercritical hydrogen combustion [29, 38], the corresponding-state method developed by Takahashi [39] is normally used for predicting the deviation from the ideal gas values. It is based on curve fitting of experimental mass diffusion coefficients of carbohydrate species. The relative product of diffusivity and pressure $(DP)_R$ is represented as function of the reduced temperature:

$$\frac{DP}{(DP)^0} = (DP)_R = (DP)_{R,l}(1 - AT_r^{-B})(1 - f) \tag{11}$$
$$f = CT_r^{-E}, \quad T_r = T / T_c$$

$(DP)^0$ is the product of diffusivity and pressure at 1 atm. $(DP)_{R,l}$, A, B, C and E are constants given in [39]. The reduced temperature T_r denotes the temperature T divide the critical temperature of the base gas. In the flame calculation, the critical temperature of the mixture is used to calculate T_r. Here the diffusivities of oxygen in water (as base gas) calculated by Takahashi formula are plotted in Fig. 3. The plot of the Takahashi model crosses the Wilke-Chang and Stokes-Einstein results at temperature lower than the critical temperature and reaches the ideal gas value at the higher temperatures. It is however observed that the calculated diffusivity is negative in the range of 0.83<Tr<0.91 and the diffusivity increases abnormally when Tr<0.83. This can be explained by the fact that most of the data employed

to produce the fitting formula are at supercritical temperature. Therefore, in this work to suppress this unphysical behaviour the diffusivity predicted by the Takahashi correlation is not used when Tr <0.93 but replaced by 0.1Dideal. In this way a continues function is obtained since the Takahashi line and the 0.1Dideal line cross at Tr=0.93.

Fig. 3 shows that at temperatures higher than 700K, there is a difference of about a factor 10 between the Takahashi model and the Wilke-Chang and Stokes-Einstein models. To the authors' knowledge there is no data available to directly judge the diffusivity prediction at this pressure and temperature range. Therefore, in Section 3 we shall study the sensitivity of predicted flame structure on the choice of mass diffusion coefficients and investigate whether the comparison of the predicted and measured flame temperature can be used to select a best diffusivity model.

2.4 Chemical mechanism

The chemical mechanism used here is a 23-species mechanism which was developed in our previous work [40] including some hydrothermal modifications upon the methanol oxidation mechanism proposed by Li et al. [41].

2.5 Numerical method

All the above mentioned hydrothermal-specific models are implemented into the 1D flame solver CHEM1D which was developed at the Eindhoven University of Technology [33]. An exponential finite-volume discretization in space is used and the resulting system is solved using a fully implicit, modified Newton technique. Adaptive gridding is implemented to increase the resolution around the flame front.

3 Results and discussion

3.1 Effect of thermodynamic and transport properties

The effect of thermodynamic and transport properties on the modeling results are investigated by implementing the modifications step by step starting from the ideal gas model. Firstly, the Peng-Robinson equation of state (PR-EOS) and the modification of enthalpy and heat capacity are implemented, which is denoted as 'Moditherm' in the following discussion. Secondly, the viscosity and thermal conductivity modifications are introduced while the mass diffusion model is kept unchanged as ideal gas (denoted as 'Moditherm&vc'). Finally, different scalings are applied on the ideal gas diffusivity to assess the sensitivity of modeling results to the diffusion model.

Fig. 4 shows the steady solutions calculated by the Ideal, Moditherm and Moditherm&vc models in the mixture fraction space, at the condition of 24wt% methanol-water mixture as fuel, pure oxygen as oxidizer, 500K inlet temperature, and 100 s^{-1} strain rate. It is to be pointed out that all the simulations conducted in this work are at the pressure of 25MPa, as default in the following. It shows that the maximum temperature after taking the PR-EOS into account decreases 294K and by the viscosity and thermal conductivity modification decreases another 106K. For density, it is observed that large difference exists at the fuel side, while at the oxidizer side the profiles almost overlap each other. It is because the critical points of fuel compositions are closer to the inlet condition than that of the oxidizer (see Table 1), and then the real-fluid effect is more prevailing at the fuel side. This regime also applies for the specific heat and thermal conductivity. When the fluid state crosses the pseudo-critical temperature, a peak value of the heat capacity appears and substantial heat is consumed. This is the main reason that the predicted temperature is 294K lower by the Moditherm model. Furthermore, the real-fluid thermal conductivity is rather large at the near-critical range, which will enhance the heat transfer from the flame zone to the colder zone. Therefore, the maximum temperature decreases 106K further by Moditherm&vc model.
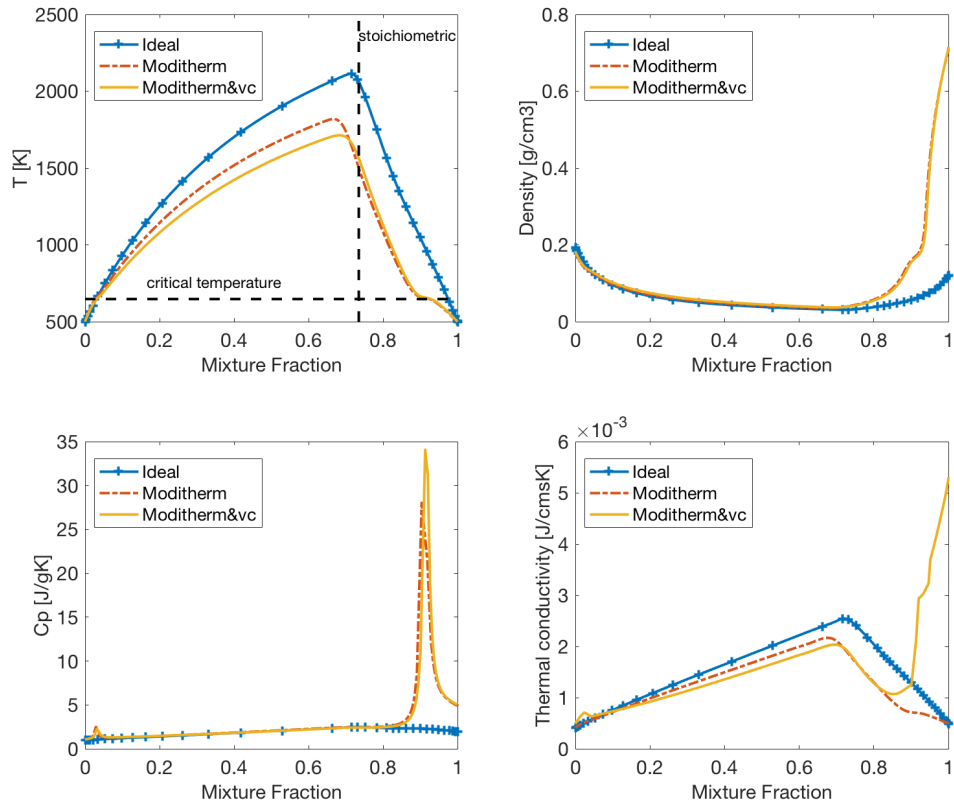
Fig. 4 Variables profiles in the mixture fraction space by different models with 24wt% methanol-water mixture as fuel and pure oxygen as oxidizer, 100 s⁻¹ strain rate and 500K inlet temperature. (top left: temperature; top right: density; bottom left: heat capacity; bottom right: thermal conductivity. Ideal: ideal gas model; Moditherm: density, enthalpy and Cp are modified by PR-EOS; Moditherm&vc: viscosity and thermal conductivity are modified additionally).

Based on the Moditherm&vc model, different scalings (0.1, 0.2, 0.5 and Takahashi) are

applied to the ideal mass diffusion model. The smallest scaling is chosen as 0.1 because the

diffusivity predicted by the Stokes-Einstein and the Wilke-Change model is in the magnitude

of the 1/10 of the ideal gas diffusivity. The calculated temperature profiles are plotted in

Temperature profiles calculated by different scalings on the mass diffusivity based on the

Moditherm&vc model. (24wt% methanol-water mixture as fuel and pure oxygen as oxidizer,

strain rate:100 s-1, inlet temperature: 700K)as well as the results from the unity Lewis number

model ($\rho D_i = \lambda C_p^{-1}$). When the inlet temperature is 700K (see Fig. 5), it shows that the

calculated temperature decreases step by step with the reduction of mass diffusivity (scaled by

0.5, 0.2, 0.1). The maximum temperature calculated by the 0.1 scaling, which represents the

Stokes-Einstein model and Wilke-Chang model, is almost 1000K lower than that by the ideal

gas model. Whereas for the Takahashi scaling, it results in nearly the same temperature profile as the ideal gas model. When the inlet temperature is 500K (see Fig. 6), the maximum temperature from Takahashi model becomes 169K lower than that from the ideal gas model. The $0.5D_{ideal}$ scaling still gives around 400K lower maximum temperature, but no converged solutions are obtained for the $0.2D_{ideal}$ and $0.1D_{ideal}$ model. This indicates that stable flames cannot be sustained at the inlet temperature of 500K, when using the $0.1D_{ideal}$ and $0.2D_{ideal}$ model.

Three points will be discussed regarding these results: 1, the mechanism how the diffusion models affect the temperature profiles; 2, the reason why the performance of Takahashi model varies with inlet temperatures; 3, the final choice of the mass diffusion model, which will be given in the next section after the comparison with experimental flame temperatures.
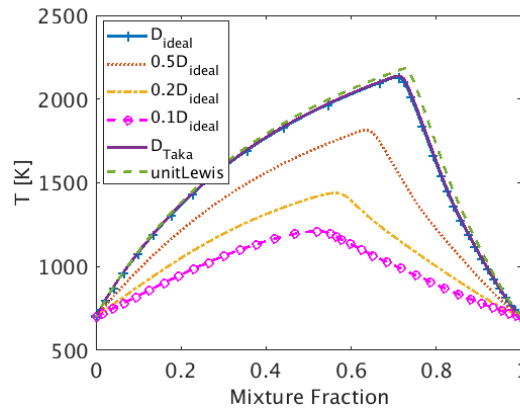

Fig. 5 Temperature profiles calculated by different scalings on the mass diffusivity based on the Moditherm&vc model. (24wt% methanol-water mixture as fuel and pure oxygen as oxidizer, strain rate:100 s^{-1}, inlet temperature: 700K)
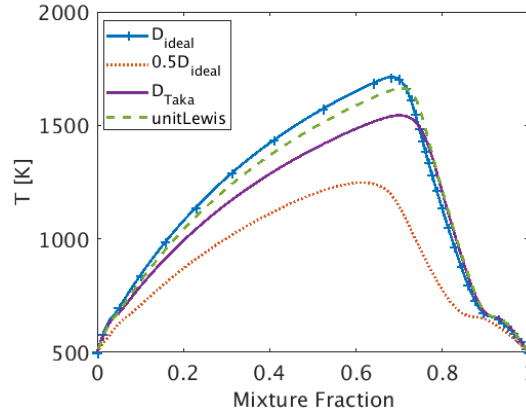
Fig. 6 Temperature profiles calculated by different scalings on the mass diffusivity based on the Moditherm&vc model. (24wt% methanol-water mixture as fuel and pure oxygen as oxidizer, strain rate:100 s⁻¹, inlet temperature: 500K)

In the steady stretched counterflow flames, the total enthalpy equation is balanced by the convection term, the enthalpy diffusion term, the preferential diffusion term and the stretch source term (see Equation (1)). Fig. 7 illustrates the four terms of the enthalpy equation resulted from different diffusion models, plotted in the physical space where positive side is oxidizer and the negative side is fuel. For the unity Lewis number case, the mass diffusion of each species is as fast as the heat transfer, so the preferential term is zero. When the ideal gas diffusion model is applied, the preferential term is nonzero because the different diffusion velocities of different species and heat. In the $0.1D_{ideal}$ case, the diffusion of species becomes ten times slower while the thermal conductivity is kept unchanged. As shown in Fig. 7 the preferential term increases one order and becomes a crucial factor in the flame zone. A more comprehensive illustration is presented in Fig. 8. It shows that the spatial spreading of temperature and main species are the same in the D_{ideal} case, while in the $0.1D_{ideal}$ case, the high-temperature zone is wider than the reaction zone. Because the heat diffusion is faster than the mass diffusion, the released heat spreads further outwards from the narrow reaction zone (also the mass mixing zone) to the outer unreacted zone. In the outer region, the stretch source term dominates the enthalpy balance and accounts for the main heat loss. This is the main reason that the calculated maximum temperature decreases with the mass diffusivity.
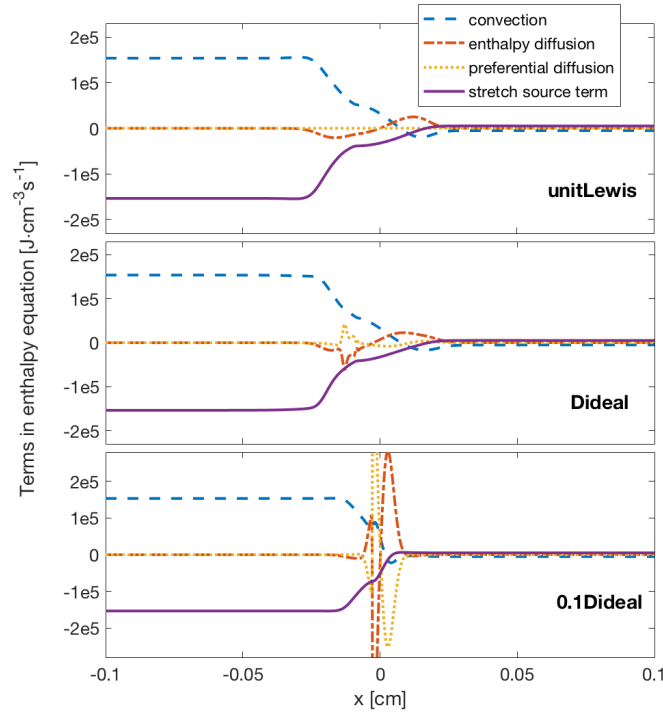
Fig. 7 The convection, enthalpy diffusion, preferential diffusion and stretch source terms in the enthalpy equation resulted from different diffusion models plotted in the physical space where fuel comes from the negative side of x axis. (24wt% methanol-water mixture as fuel and pure oxygen as oxidizer, strain rate:100 s^{-1}, inlet temperature: 700K)
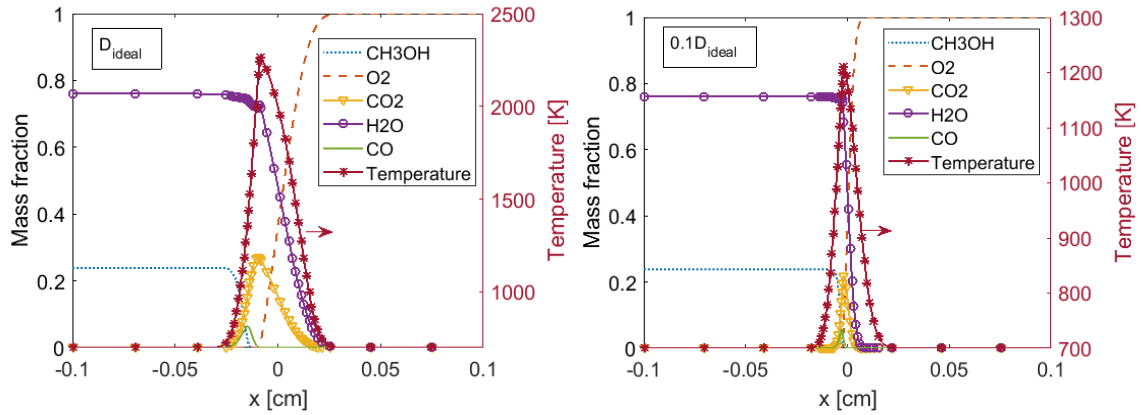

Fig. 8 Species and temperature profiles plotted in the physical space where fuel comes from the negative side of x axis, resulted from two diffusion models, left: the ideal gas diffusion model; right: 0.1 scaling on the ideal gas diffusivity (24wt% methanol-water mixture as fuel and pure oxygen as oxidizer, strain rate:100 s^{-1}, inlet temperature: 700K).

Contrasting with this, the Takahashi diffusion model only shows a limited effect on the calculated temperature profiles (as shown in Fig 5 and Fig 6). This is because the Takahashi scaling is temperature-dependent rather than a constant. As shown in Fig. 3, it is nearly the same as the ideal gas model when temperature is higher than 1000K, and it decreases to

0.1Dideal at about 600K, where T_r=0.93 as discussed in *section 2.3.2 Mass diffusivity*. Therefore, the higher the inlet temperature is, the closer the results are to the ideal gas model results. In the main flame zone where temperature is higher than 1000K, the Takahashi diffusion scaling does not have any effect on the results.

3.2 Comparisons with the ETH hydrothermal flame experiments

3.2.1 Flame temperature

Wellig et al.[12] have realised methanol hydrothermal flames in a co-flow combustor and measured the flame temperature using thermocouple at different fuel concentrations and inlet temperatures. According to the flamelet theory, the local structures of co-flow diffusion flame can be presented by laminar counterflow flames which share the same inlet conditions. By solving the transport equation of mixture fraction in the real flow field, the local temperature can be determined as function of the local mixture fraction and flow condition (strain rate/scalar dissipation rate). To evaluate the developed models, especially to find the most suitable mass diffusion model, we conducted two cases with the same inlet conditions as the experiments of Wellig et al. The calculated flame temperatures by different models and the experimental value are listed in Table 2.

Firstly, models that do not predict existence of a flame for a condition where a flame exists in experiment must be discarded. This is the case for the $0.1D_{ideal}$ model and the $0.2D_{ideal}$ model. As shown in Table 2, the 0.1Dideal model and the 0.2Dideal model cannot predict a stable flame at the inlet temperature of 510K for fuel and 584K for oxidizer, while experimentally a stable flame exists with temperature 1241K at the same inlet condition. Then based on the analysis in Section 2.3.2 also the Wilke-Chang and Stokes-Einstein models are not appropriate to simulating the hydrothermal flame.

Secondly, when presence of a flame is predicted in agreement with experiment, the question arises which temperature in a counterflow flame is the best choice for the comparison with the experimental data. Three choices can be made corresponding to three typical mixture fractions: the maximum temperature position Z_{max}, the stoichiometric position Z_{sto} (0.735 for 24wt% methanol) and the mixture fraction when the experimental fuel and oxidizer stream (stoichiometric oxygen excess is 1.2 [12]) are perfectly mixed (Z_{out}=0.698). As shown in Table 2, the calculated temperature at Z_{out} is mostly larger than that at Z_{sto} except for the results by the unity Lewis model. This is because that the diffusion is faster in the oxidizer side than the fuel side and hence the flame position is closer to the oxidizer side. According to Wellig et al.[12], the flame temperature is detected by a thermocouple which is located 12mm below the end of the combustion chamber. The combustion chamber is 50mm long below the nozzle, which may be long enough for the development of the flame. On the other hand, the diameter of the thermocouple is 1mm which may be larger than the flame thickness and result to an average temperature of the flame front. Therefore, it is an acceptable choice to use the temperature at Z_{out} as the reference value to be compared with the experimental flame temperature.

Lastly, there are some factors that will cause the calculated temperature higher than the experimental flame temperature: the heat loss through the cooling wall is not considered in the adiabatic calculation of counterflow flames; the thermocouple may be not located in the fully developed flame zone; the turbulent fluctuation of the local mixture fraction and strain rate will lead the turbulent flame temperature lower than the laminar flame temperature. The strain rate applied for the calculations in Table 2 is 100 s^{-1}. In the practical combustor, the local strain rate is affected by the local turbulent fluctuation and the strain rate itself is also fluctuated. Fig. 9 shows the calculated temperature profiles at different strain rates. The differences in maximum temperature due to strain rate change are about 100K at inlet

temperature of 500K and 400K at inlet temperature of 700K. Hence it is expectable that the turbulent fluctuation may cause the experimental flame temperature approximately 100K lower than the calculated counterflow flame temperature.

According to the above discussion, the $0.5D_{ideal}$ model is also eliminated because its predicted flame temperature at Z_{out} for case 2 (shown in Table 2) is about 100 K lower than the experimental value. The Takahashi model is proved to be an appropriate model for the hydrothermal flames, by which the predicted flame temperature is approximately 300-500K higher than the experimental flame temperature, in a reasonable range considering all the factors discussed in the previous paragraph.

Table 2 Comparison of calculated counterflow flame temperatures and the experimental flame temperatures. (24wt%methanol/water as fuel, pure oxygen as oxidizer and the strain rate is 100 s^{-1}).

Case 1		Fuel: 24wt% methanol-water, 694K; Oxidizer: pure oxygen, 635K						
		D_{ideal}	unitLewis	D_{Taka}	$0.5D_{ideal}$	$0.2D_{ideal}$	$0.1D_{ideal}$	Exp*
Flame Temperature**(K)	at Z_{max}	2113	2166	2121	1792	1410	1178	
	at Z_{sto}	2038	2149	2042	1448	1101	947	1497
	at Z_{out}	2113	2142	2113	1597	1166	988	
Case 2		Fuel: 24wt% methanol-water, 510K; Oxidizer: pure oxygen,584K						
		D_{ideal}	unitLewis	D_{Taka}	$0.5D_{ideal}$	$0.2D_{ideal}$	$0.1D_{ideal}$	Exp
Flame Temperature(K)	at Z_{max}	1734	1694	1588	1287			
	at Z_{sto}	1575	1656	1561	1026	N***	N	1261
	at Z_{out}	1727	1691	1587	1171			

*Exp: Experimental data obtained from Table 6 (T$_1$ for flame temperature; T$_{bn}$ for inlet temperature of fuel; T$_{an1}$ for inlet temperature of oxygen) in Ref. [12], which is detected by a thermocouple located on axis 12 mm below the combustion chamber. The deviation of T$_1$ is ±25°C obtained from Fig. 10 in [12].

**Flame temperature by calculation is presented at three different mixture fraction positions: Z$_{max}$, Z$_{sto}$, Z$_{out}$ (details see the text).
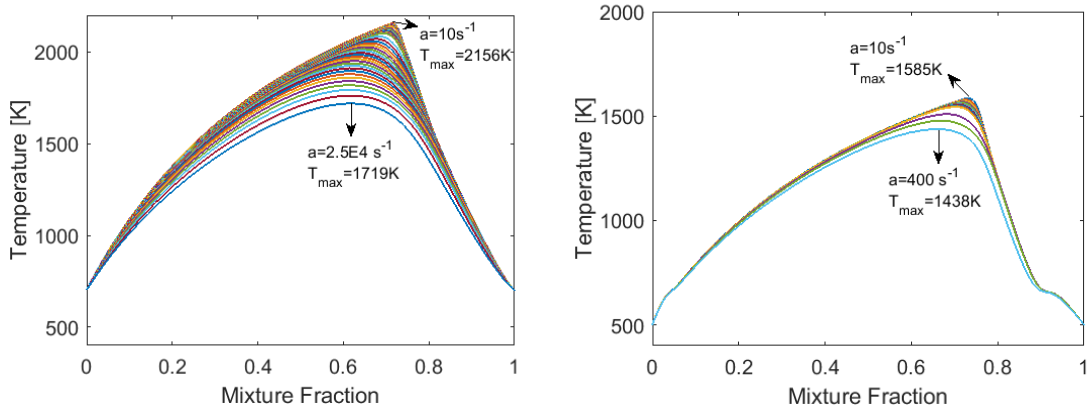
***N: no flame can be sustained at this condition.

Fig. 9 Temperature profiles at different strain rates (from 10s⁻¹ to the extinction strain rate), 24wt% methanol/water as fuel, pure oxygen as oxidizer, inlet temperature: 700K (left); 500K (right).

3.2.2 Length scale of the hydrothermal flame

The turbulence intensity will determine the local fluctuation and hence affect the flame structure. In the following part, the length scale of the laminar counterflow flame will be compared with the turbulence length scale in the ETH hydrothermal flame reactor to judge the practical turbulence intensity.

For the ETH hydrothermal flame setup, the turbulent dissipation rate ε at the flame front is about 20 m^2/s^3 which can be calculated by our preliminary 2-D model [19]. Then the Kolmogorov Length Scale l_k can be estimated as 0.01 mm with the formula $l_k = (\frac{\nu^3}{\varepsilon})^{1/4}$, where ν is the kinetic viscosity ($\approx$6E-7 m^2/s). However, the calculated flame thickness of the laminar counterflow flame is 0.13mm by OH and 0.42mm by temperature (see Fig. 10). The chemical length scale is ten times larger than the smallest turbulence length scale, indicating that the turbulence would affect the flame intensively.

At such intensive turbulence condition, the turbulent transport will weaken the differential diffusion effects. This has been observed previously in gaseous flames at atmospheric pressure. Ramaekers et al. [21] had conducted a priori test of different FGM tables on the Sandia Flames [42], showing that the unity Lewis number model can predict more accurate mass fraction of species than the multi-component diffusion model, especially at high

turbulence intensity. Similar results were also observed by Barlow [42]. Therefore, the differential diffusion of mass and heat, which leads to the decrease in the flame temperature as discussed in section 3.1, could play a smaller role in the turbulent flow reactor than in the laminar counterflow diffusion flame. This should be explored further in turbulent combustion simulations.
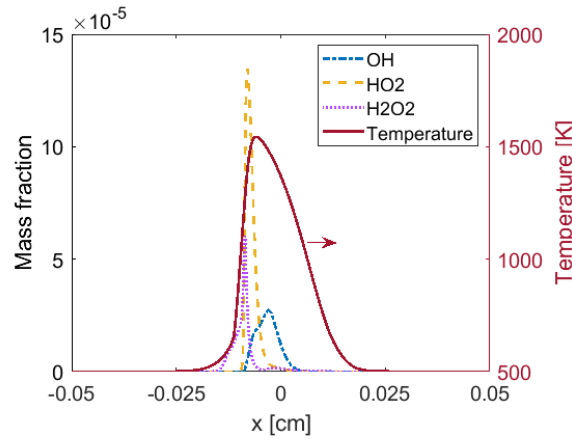

Fig. 10 Mass fraction of radicals as well as the temperature profiles in the physical space where fuel comes from the negative side of x axis (24wt%methanol-water as fuel, inlet temperature 500K).

3.2.3 Flame stability

The flame stability is always a key issue in hydrothermal combustion. Wellig et al. [12] have tested the extinction temperature of methanol hydrothermal flames for different methanol concentration. Using the developed hydrothermal counterflow flame model, the maximum temperatures calculated at different methanol concentration, inlet temperature and strain rate are plotted in Fig. 11. It shows that the maximum temperature decreases with the decrease in methanol concentration and inlet temperature. This trend agrees well with the experimental results [12]. If the calculated maximum temperature is the same as the inlet temperature, it means that the steady hydrothermal flame cannot be sustained at this condition.

At specific methanol concentration and inlet temperature, there exists an extinction strain rate. The smallest strain rate calculated in this work is 10 s^{-1}. If the flame cannot be sustained at 10 s^{-1}, we conclude that a steady flame cannot exist at this specific methanol concentration and

inlet temperature condition. In this way, a stable flame zone is obtained as visualized in Fig. 11. It is validated that the calculated stable flame zone can cover the experimental extinction conditions, which are 693K, 563K and 456K inlet temperature at 8wt%, 16wt% and 24wt% methanol concentration respectively [12]. Besides, the calculated stable flame zone extends to lower inlet temperatures. This is reasonable because the experimental flow condition determined the local strain rate and lower extinction temperature can only be achieved at lower strain rate. According to the calculated stable flame zone, the corresponding extinction strain rate at experimental extinction conditions are 50-100 s^{-1} varying with inlet temperatures.
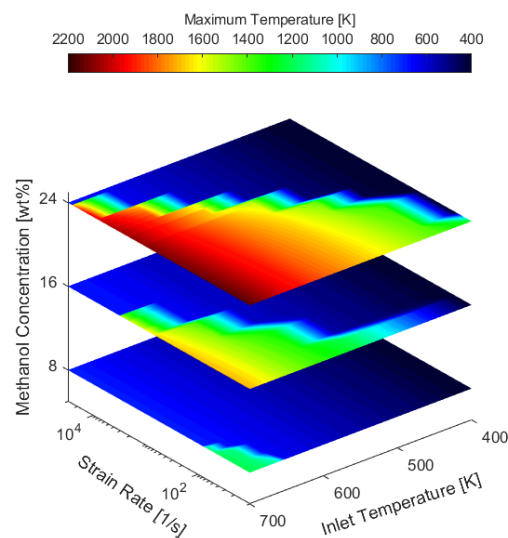

Fig. 11 The maximum temperature in the counterflow hydrothermal methanol flames as function of methanol concentration, inlet temperature and strain rate.

3.3 Generation of the FGM table

One important aim of a counterflow flame study is to generate flamelet or FGM (Flamelet Generated Manifold) table, which can be used in the multi-dimensional turbulent flame simulations. Flamelet or FGM table includes flame structure based on detailed chemistry and transport. The unclosed chemical source terms appearing in turbulence modelling approaches can be closed by the probability-weighted average of the dependent variable obtained from

the table. The main difference between the classic flamelet tabulation and the FGM tabulation is how they account for the non-equilibrium effects. In the classic flamelet model, the non-equilibrium state is considered due to the flame stretch only. Whereas in the FGM model, the non-equilibrium states during the ignition or extinction process are tabulated together with the steady stretched flamelets to account for the highly non-equilibrium effects. Considering the intensive turbulence-chemistry interaction indicated above and the interested ignition and extinction conditions, the FGM tabulation method is chose in this work.

To establish the FGM table, unsteady counterflow flames are calculated to account for the highly non-equilibrium conditions, besides the steady cases. As an example, we consider the case of 24wt% methanol as fuel with 530K inlet temperature and pure oxygen as oxidizer with 590K inlet temperature. Firstly, steady calculations are conducted from the strain rate of 10 s^{-1} until the extinction strain rate, which is resulted to be 940 s^{-1}. Then unsteady counterflow flames are calculated at strain rate of 950 s^{-1} with the results at 940 s^{-1} as the initial solution. Fig. 12 shows the calculated temperature profiles at both steady and unsteady conditions. It indicates that the combination of the steady and unsteady counterflow flame results can cover the full thermochemical states from unburned to quasi-equilibrium.
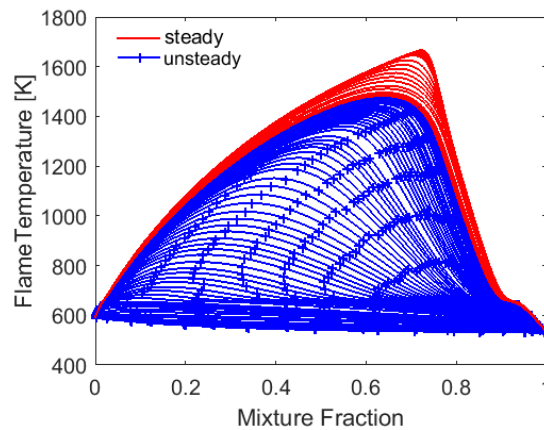

Fig. 12 Temperature profiles of steady and unsteady counterflow flames (fuel inlet: 530K, 24wt% methanol/water; oxidizer inlet: 590K, pure oxygen; strain rate: 10-950 s^{-1}).

The FGM table uses a progress variable as the second independent variable, while mixture fraction is the first one. The progress variable is usually defined as a linear combination of a set of species mass fraction, which can be conveniently solved in a transport equation during multi-dimensional simulation. Following this definition, the un-normalized progress variable Y_c and normalized progress variable c is formulated as:

$$Y_c = \sum \alpha_i Y_i \tag{12}$$

$$c = \frac{Y_c - Y_{c,min}}{Y_{c,max} - Y_{c,min}} \tag{13}$$

in which α_i is the weighting coefficient for species i, Y_i is the mass fraction of species i and $Y_{c,max}$, $Y_{c,min}$ are the maximum and minimum Y_c at fixed mixture fraction respectively. Ramaekers et al. [21] suggested that α_i equal to the inverse of the molar mass of species i ($\alpha_i = 1/\omega_i$) ensures a monotonous increasing Y_c for all flamelets used, which is adopted in this work. The selection of the species set from which the progress variable is constructed will influence the model performance, in the sense of uniquely characterizing each point in the thermochemical state space [43]. Hence we tested the un-normalized progress variables based on different sets of species. As shown in Fig. 13, when adding CO, H_2, H_2O into the species set, crossings of the progress variable curves occur, especially at the oxidizer side, which will lead to inaccuracy in determining the thermochemical state. This is caused by large difference in rate of change of the different species in different regions of the mixture fraction space. Fig. 14 illustrates the species mass fraction as function of mixture fraction. It shows that the mass fraction of CO is only observably nonzero when mixture fraction is larger than 0.7. On the other hand, the mass fraction of water is nearly unchanged at the fuel side, because it is a main component of the fuel. Therefore, to generate a correct and useful FGM table for the studied hydrothermal flames, we only use CO_2 to define the un-normalized progress variable.
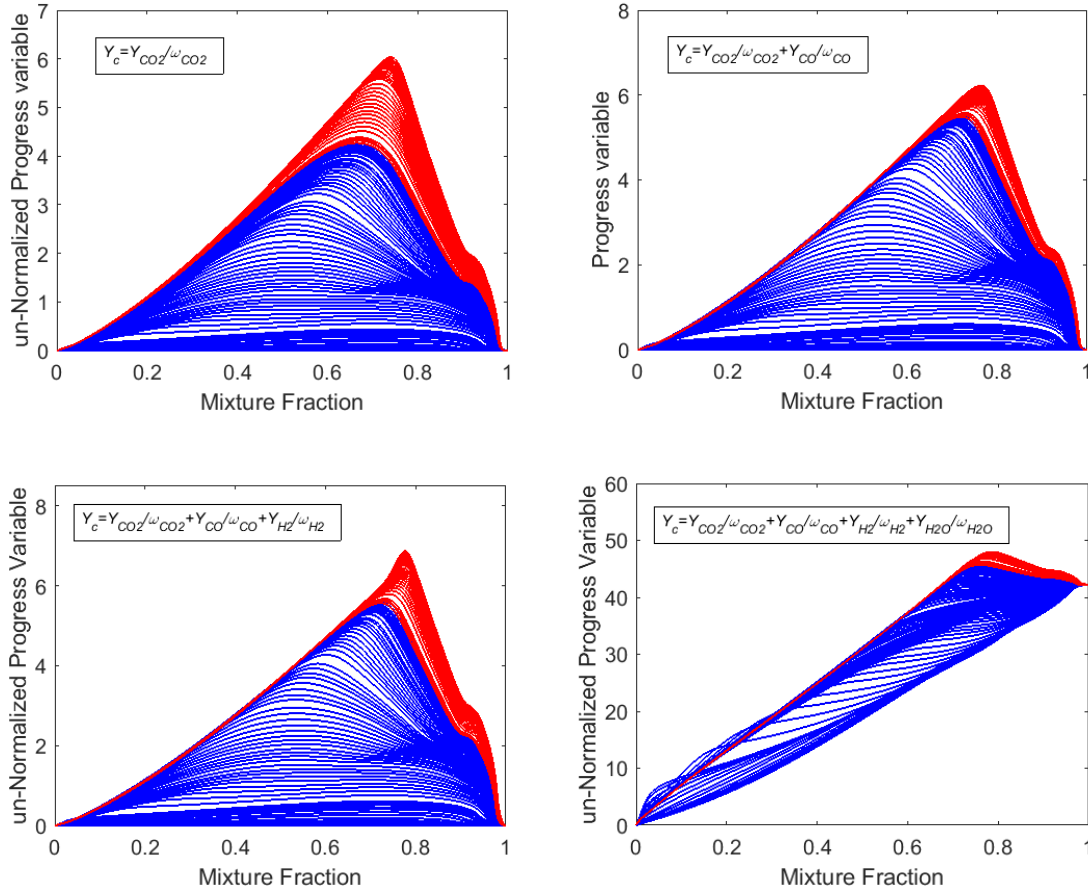
Fig. 13 Performance of progress variables defined by different species set (fuel inlet: 530K, 24wt% methanol/water; oxidizer inlet: 590K, pure oxygen; from 80 steady counterflow flames and 83 unsteady counterflow flames).
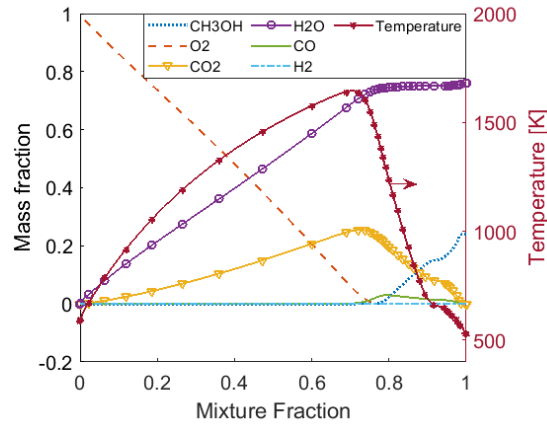

Fig. 14 Species and temperature profiles in the mixture fraction space (fuel inlet: 530K, 24wt% methanol/water; oxidizer inlet: 590K, pure oxygen; strain rate: 100 s^{-1}).

In this way, from 80 steady counterflow flames and a set of 83 states of an unsteady counterflow flame, an FGM table is generated, which is partially visualized in Fig. 15. All species mass fraction and thermodynamic properties are tabulated in the mixture fraction and

normalized progress variable space, as well as the source term of the progress variable. The constructed FGM can be implemented into a multi-dimensional turbulent flame simulation case, providing the detailed flame information. An assumed or calculated probability density function (PDF) of the independent variables will be introduced to account for the turbulent fluctuation. Such method however does not directly include the disturbance of the flame structure by the Kolmogorov scale eddies. Whether or not this would have strong impact on mean flame temperature is a topic of further investigation.
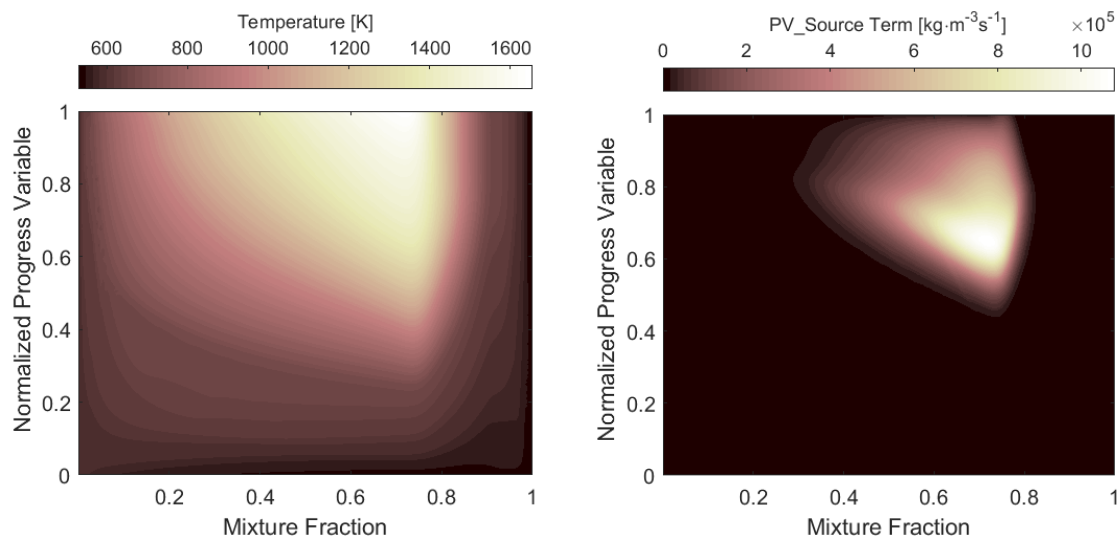

Fig. 15 Visualization of the FGM table (left: temperature; right: source term of progress variable; fuel inlet: 530K, 24wt% methanol/water; oxidizer inlet: 590K, pure oxygen; from 80 steady counterflow flames and 83 unsteady counterflow flames)

4   Conclusion

A hydrothermal flame is characterized by a relatively low flame temperature due to the special thermodynamic and transport properties of the supercritical fluid. The density, heat capacity and thermal conductivity all increase dramatically near the pseudo-critical temperature. Each of these properties leads to flame temperature being lower than the values calculated by the ideal gas assumption. The sum of the discrepancies is up to 400K in the maximum flame temperature for the case of 24wt% methanol-water as fuel, pure oxygen as oxidizer and inlet temperature of 500K. The flame temperature is also sensitive to the mass

diffusion coefficients. The decrease in mass diffusivity will decrease the flame temperature because of the preferential diffusion of heat over species. Based on comparison with the ETH experimental thermocouple measurements of flame temperature the corrected Takahashi diffusion model is found to describe this effect. The calculated flame temperature reasonably agrees with the experimental data, considering the uncertainty on possible heat loss and impact of turbulent fluctuations and the limited spatial resolution of a thermocouple. The model predictions of the dependence of the flame stability on methanol concentration and inlet temperature can also be validated. The calculated stable combustion zone covers the ETH experimental extinction conditions and presents the possibility of achieving the lower extinction temperatures by adjusting the flow field to the strain rate lower than 50 s^{-1}.

The effect of turbulence can be estimated on the basis of comparison of length scales. The thickness of the laminar counterflow flame is found to be ten times larger than the Kolmogorov length scale of the practical flow field in the ETH combustor, which means that the turbulence affects the flame structure. It means that the sensitivity of the flame to the mass diffusion model would be damped by the presence of the turbulent transport.

An FGM table is generated from 80 steady counterflow flames and a series of 83 states of an unsteady counterflow flame. By including the transient results during the extinction process, this FGM table can cover the whole range of thermochemistry states, from the unburned state to the least stretched state. Using only CO_2 to construct the progress variable without adding other species is shown to be a good choice for this hydrothermal flame. The source term of the progress variable as well as all the thermochemistry variables are tabulated. This hydrothermal FGM table will be used to simulate the turbulent hydrothermal flames in our forthcoming work.

5 Acknowledgements

6   References

[1] C. Augustine, J.W. Tester, Hydrothermal flames: From phenomenological experimental demonstrations to quantitative understanding, J. Supercrit. Fluids, 47 (2009) 415-430.

[2] W. Schilling, E.U. Franck, Combustion and Diffusion Flames at High Pressures to 2000 bar, Berichte der Bunsengesellschaft für physikalische Chemie, 92 (1988) 631-636.

[3] A. Kruse, H. Vogel, Heterogeneous catalysis in supercritical media: 2. Near-critical and supercritical water, Chem. Eng. Technol., 31 (2008) 1241-1245.

[4] G. Brunner, Near and supercritical water. Part II: Oxidative processes, Journal of Supercritical Fluids, 47 (2009) 382-390.

[5] P.A. Marrone, Supercritical water oxidation-Current status of full-scale commercial activity for waste destruction, Journal of Supercritical Fluids, 79 (2013) 283-288.

[6] S.N. Reddy, S. Nanda, U.G. Hegde, M.C. Hicks, J.A. Kozinski, Ignition of hydrothermal flames, Rsc Advances, 5 (2015) 36404-36422.

[7] M.D. Bermejo, P. Cabeza, J.P.S. Queiroz, C. Jimenez, M.J. Cocero, Analysis of the scale up of a transpiring wall reactor with a hydrothermal flame as a heat source for the supercritical water oxidation, Journal of Supercritical Fluids, 56 (2011) 21-32.

[8] P.R. Von Rohr, K. Prikopsky, T. Rothenfluh, Flames in supercritical water and their applications, Stroj. Cas., 59 (2008) 91-103.

[9] J. Zhang, S. Wang, M. Ren, J. Lu, S. Chen, H. Zhang, Effect Mechanism of Auxiliary Fuel in Supercritical Water: A Review, Industrial & Engineering Chemistry Research, 58 (2019) 1480-1494.

[10] J.P.S. Queiroz, M.D. Bermejo, M.J. Cocero, Kinetic model for isopropanol oxidation in supercritical water in hydrothermal flame regime and analysis, Journal of Supercritical Fluids, 76 (2013) 41-47.

[11] M.D. Bermejo, C. Jimenez, P. Cabeza, A. Matias-Gago, M.J. Cocero, Experimental study of hydrothermal flames formation using a tubular injector in a refrigerated reaction chamber. Influence of the operational and geometrical parameters, Journal of Supercritical Fluids, 59 (2011) 140-148.

[12] B. Wellig, M. Weber, K. Lieball, K. Príkopský, P. Rudolf von Rohr, Hydrothermal methanol diffusion flame as internal heat source in a SCWO reactor, J. Supercrit. Fluids, 49 (2009) 59-70.

[13] B. Wellig, K. Lieball, P. Rudolf von Rohr, Operating characteristics of a transpiring-wall SCWO reactor with a hydrothermal flame as internal heat source, J. Supercrit. Fluids, 34 (2005) 35-50.

[14] R.M. Serikawa, T. Usui, T. Nishimura, H. Sato, S. Hamada, H. Sekino, Hydrothermal flames in supercritical water oxidation: investigation in a pilot scale continuous reactor, Fuel, 81 (2002) 1147-1159.

[15] C. Narayanan, C. Frouzakis, K. Boulouchos, K. Príkopský, B. Wellig, P. Rudolf von Rohr, Numerical modelling of a supercritical water oxidation reactor containing a hydrothermal flame, J. Supercrit. Fluids, 46 (2008) 149-155.

[16] J. Sierra-Pallares, M. Teresa Parra-Santos, J. García-Serna, F. Castro, M. José Cocero, Numerical modelling of hydrothermal flames. Micromixing effects over turbulent reaction rates, J. Supercrit. Fluids, 50 (2009) 146-154.

[17] L.K. Hjertager, B.H. Hjertager, T. Solberg, CFD modelling of fast chemical reactions in turbulent liquid flows, Computers & Chemical Engineering, 26 (2002) 507-515.

[18] J.P.S. Queiroz, M.D. Bermejo, M.J. Cocero, Numerical study of the influence of geometrical and operational parameters in the behavior of a hydrothermal flame in vessel reactors, Chemical Engineering Science, 112 (2014) 47-55.

[19] M. Ren, S. Wang, C. Yang, Ignition and Extinction Modeling of Hydrothermal Flames, in: H. Hou, Z. Han (Eds.) Proceedings of the 2017 5th International Conference on Machinery, Materials and Computing Technology, Atlantis Press, Paris, 2017, pp. 439-443.

[20] E. Mastorakos, Ignition of turbulent non-premixed flames, Progress in Energy and Combustion Science, 35 (2009) 57-97.

[21] W.J.S. Ramaekers, J.A. van Oijen, L.P.H. de Goey, A Priori Testing of Flamelet Generated Manifolds for Turbulent Partially Premixed Methane/Air Flames, Flow, Turbulence and Combustion, 84 (2010) 439-458.

[22] C. Bajaj, M. Ameen, J. Abraham, Evaluation of an Unsteady Flamelet Progress Variable Model for Autoignition and Flame Lift-Off in Diesel Jets, Combustion Science and Technology, 185 (2013) 454-472.

[23] E. Abtahizadeh, P. de Goey, J. van Oijen, Development of a novel flamelet-based model to include preferential diffusion effects in autoignition of CH4/H2 flames, Combustion and Flame, 162 (2015) 4358-4369.

[24] J.A. van Oijen, A. Donini, R.J.M. Bastiaans, J.H.M. ten Thije Boonkkamp, L.P.H. de Goey, State-of-the-art in premixed combustion modeling using flamelet generated manifolds, Progress in Energy and Combustion Science, 57 (2016) 30-74.

[25] S.B. Pope, Small scales, many species and the manifold challenges of turbulent combustion, Proceedings of the Combustion Institute, 34 (2013) 1-31.

[26] N.A.N. Zong, V. Yang, CRYOGENIC FLUID JETS AND MIXING LAYERS IN TRANSCRITICAL AND SUPERCRITICAL ENVIRONMENTS, Combustion Science and Technology, 178 (2006) 193-227.

[27] J.C. Oefelein, Mixing and combustion of cryogenic oxygen-hydrogen shear-coaxial jet flames at supercritical pressure, Combustion Science and Technology, 178 (2006) 229-252.

[28] S. Candel, M. Juniper, G. Singla, P. Scouflaire, C. Rolon, STRUCTURE AND DYNAMICS OF CRYOGENIC FLAMES AT SUPERCRITICAL PRESSURE, Combustion Science and Technology, 178 (2006) 161-192.

[29] G. Ribert, N. Zong, V. Yang, L. Pons, N. Darabiha, S. Candel, Counterflow diffusion flames of general fluids: Oxygen/hydrogen mixtures, Combustion and Flame, 154 (2008) 319-330.

[30] G. Lacaze, J.C. Oefelein, A non-premixed combustion model based on flame structure analysis at supercritical pressures, Combustion and Flame, 159 (2012) 2087-2103.

[31] Z. Gao, H. Wang, K. Luo, C. Song, C. Zhao, J. Xing, J. Fan, Evaluation of real-fluid flamelet/progress variable model for laminar hydrothermal flames, J. Supercrit. Fluids, 143 (2019) 232-241.

[32] W. Ramaekers, Development of flamelet generated manifolds for partially-premixed flame simulations, in, Technische Universiteit Eindhoven Eindhoven, 2011.

[33] L. Somers, The simulation of flat flames with detailed and reduced chemical models, Eindhoven University of Technology, Eindhoven, (1994).

[34] A. Evlampiev, Numerical Combustion Modeling for Complex Reaction Systems, in, Technische Universiteit Eindhoven, Eindhoven, 2007.

[35] D.-Y. Peng, D.B. Robinson, A new two-constant equation of state, Industrial & Engineering Chemistry Fundamentals, 15 (1976) 59-64.

[36] http://webbook.nist.gov/cgi/fluid.cgi?ID=C7732185&Action=Page in, National Institute of Standards and Technology, Gaithersburg.

[37] S. Kraft, F. Vogel, Estimation of Binary Diffusion Coefficients in Supercritical Water: Mini Review, Industrial & Engineering Chemistry Research, 56 (2017) 4847-4855.

[38] W. Liang, W. Li, C.K. Law, Laminar flame propagation in supercritical hydrogen/air and methane/air mixtures, Proceedings of the Combustion Institute, (2018).

[39] S. Takahashi, PREPARATION OF A GENERALIZED CHART FOR THE DIFFUSION COEFFICIENTS OF GASES AT HIGH PRESSURES, Journal of Chemical Engineering of Japan, 7 (1975) 417-420.

[40] M. Ren, S. Wang, J. Zhang, Y. Guo, D. Xu, Y. Wang, Characteristics of Methanol Hydrothermal Combustion: Detailed Chemical Kinetics Coupled with Simple Flow Modeling Study, Industrial & Engineering Chemistry Research, 56 (2017) 5469-5478.

[41] J. Li, Z. Zhao, A. Kazakov, M. Chaos, F.L. Dryer, J.J. Scire, A comprehensive kinetic mechanism for CO, CH2O, and CH3OH combustion, International Journal of Chemical Kinetics, 39 (2007) 109-136.
[42] R.S. Barlow, J.H. Frank, A.N. Karpetis, J.Y. Chen, Piloted methane/air jet flames: Transport effects and aspects of scalar structure, Combustion and Flame, 143 (2005) 433-449.
[43] M. Ihme, Y.C. See, Prediction of autoignition in a lifted methane/air flame using an unsteady flamelet/progress variable model, Combustion and Flame, 157 (2010) 1850-1862.